



Dynamic recrystallization mechanism, grain structure evolution, and mechanical behavior in friction stir welding of galvanized steel at different cooling rates

Tao Sun¹ · Jianhui Wu¹ · Zhihui Yang² · Wang Ge³ · Guoqiang Huang¹ · Yifu Shen¹ 

Received: 14 June 2023 / Accepted: 30 March 2024 / Published online: 3 May 2024
© The Author(s), under exclusive licence to Springer-Verlag London Ltd., part of Springer Nature 2024

Abstract

Friction stir welding (FSW) of galvanized steel offers unique advantages as it can avoid the extensive metallurgical problems associated with fusion welding. However, conventional FSW still leads to a higher temperature in the stir zone, which deteriorates the microstructure. To obtain a satisfactory weld, the welded joints of galvanized steel were created by FSW with different cooling rates employing a W–Re rotary tool with a large-diameter needle. The correlation between the microstructure evolution and mechanical behavior of joints at different cooling rates was systematically studied. The results demonstrate that the rapid cooling rate favors the refinement of ferrite and diffuse distribution of Fe₃C. In addition, weakening of the texture and dispersion of dislocations were also observed after fast cooling FSW. It can be concluded that the microstructural evolution mechanism of the stirring zone (SZ) is continuous dynamic recrystallization at a slow cooling rate, while the microstructure has discontinuous dynamic recrystallization as the primary evolution mechanism at a fast cooling rate. Based on these advantages, the tensile specimens with fast cooling FSW obtained a synergistic improvement in strength-ductility, even surpassing the base material. This work provides new ideas for welding galvanized steel.

Keywords Friction stir welding · Galvanized steel · Recrystallization · Microstructure · Mechanical properties

1 Introduction

Stainless steel, with excellent corrosion resistance and mechanical properties, is becoming more and more widely used [1, 2], but its high price leads to higher economic costs. In contrast, cheap galvanized steel is a metallic material obtained by galvanizing plain carbon steel, which provides excellent corrosion resistance and mechanical properties. Therefore, it is a widely used material for automotive

structures [3]. However, the weldability is much less than that of common steel because the presence of the galvanized layer will make galvanized steel produce porosity and spatter during the welding, which will reduce the quality of the products [4, 5]. In addition, high temperatures and toxic fumes can be harmful to the operator's health.

Current research on the welding of galvanized steel is focused on the protection of welding equipment, defect detection, and defect prediction. For example, Xing et al. [6] found that resistance welding of galvanized steel leads to a significant reduction in electrode life, which they successfully predicted through qualitative and quantitative analysis. Zdravecká et al. [7] analyzed the mechanism of porosity formation in galvanized steel during laser welding and found that process parameters have a strong influence on the quality of galvanized steel welding. Ma et al. [8] proposed a method for detecting defects in galvanized steel welds based on active visual perception and machine learning, which is of great help for robotic welding manufacturing. Wan et al. [4] developed a thermal fluid numerical model to successfully predict spatter in thin galvanized steel sheets during laser welding. Although these studies have provided

✉ Guoqiang Huang
gqhuang1105@gmail.com

✉ Yifu Shen
shenyifu0501@gmail.com

¹ College of Materials Science and Technology, Nanjing University of Aeronautics and Astronautics, 29 Jiangjun Road, Nanjing 210016, People's Republic of China

² Nantong Institute of Technology, 211 Yongxing Road, Nantong 226002, People's Republic of China

³ Engineering Training Center, Nanjing University of Aeronautics and Astronautics, 29 Jiangjun Road, Nanjing 210016, People's Republic of China

numerous improvements to the welding of galvanized steel, they have not addressed the root cause of the welding problems in galvanized steel. In this context, friction stir welding (FSW), a new solid phase joining technique, can be a perfect solution to these problems [9]. In addition, the narrow heat-affected zone (HAZ) is uniformly homogeneous with the base material (BM) and the weld often has more perfect microstructures and properties as a modified zone.

FSW of low melting point materials (aluminum alloys, magnesium alloys, polymers, etc.) has achieved impressive success and commercial applications in the last decades. For example, Bagheri et al. [10] used the Taguchi method to optimize the FSW parameters for AA6061-T6 aluminum alloy and combined it with numerical simulations to verify that the joints prepared with the optimum parameters were more satisfactory. Adibeig et al. [11, 12] explored the effect of process parameters on the mechanical properties of polymer FSW joints, and the results showed that FSW is suitable for thermoplastics, which provides a new joining method for polymers. Schmidt et al. [13, 14] were the first to investigate the temperature field and flow field characteristics of aluminum alloys during FSW, and they gave methods to evaluate the material flow velocity through experiments and numerical simulations. These works have provided a solid theoretical basis for expanding the industrial applications of FSW. With the gradual systematization of FSW-related research, FSW-derived technologies such as friction stir processing [15], friction stir vibration welding (FSVW) [16, 17], and friction stir vibration processing (FSVP) [18] have emerged. The Abbasi team [19, 20] recently implemented FSVW and finite element analysis on magnesium and aluminum alloys. The results showed that FSVW is beneficial in increasing the dislocation density in the weld zone and promoting grain refinement. In addition, they prepared aluminum matrix composites by FSVP [18]. The results showed that the FSVP helped to improve the microstructure and the second-phase distribution, which resulted in a synergistic enhancement of wear resistance and corrosion resistance.

Recently, some researchers have performed FSW by increasing the cooling rate [21–23] to prepare more perfect welds. The main advantages include two aspects: (I) a significant reduction in the peak welding temperature and (II) further refinement of the microstructure and regulation of precipitates. Abbasi et al. [21] investigated the effect of the welding environment on the dynamic recrystallization (DRX) and residual stress during FSW of aluminum alloys. The results showed that the water-cooled environment is conducive to exacerbating the DRX and effectively inhibiting the growth of the grains and increasing residual compressive stresses, which resulted in the synergistic improvement of the strength and the ductility. Bagheri et al. [22] studied FSW of 6061 aluminum alloy using smooth particle hydrodynamics (SPH) numerical analysis. They found that underwater

welding resulted in better cooling, lower peak temperatures, and higher stress distributions compared to conventional welding. Luo et al. [23] used CO₂-assisted FSW to weld 7075 fine-grained aluminum alloy and obtained significant grain refinement and satisfactory mechanical properties.

Although the FSW of high melting point materials has not been developed to the level of low melting point materials, some excellent research results have been achieved for the FSW of steel. For example, Cao et al. [24] successfully prepared ultra-fine-grain duplex stainless steel joints by underwater FSW. They found that the water-cooled environment promotes a more uniform and balanced distribution of α and β phases, which leads to a synergistic increase in strength-plasticity. Wang et al. [25] investigated in detail the microstructure evolution of TRIP steel after FSW. They concluded that martensitic transformation occurs in the stirring zone (SZ) and thermos-mechanically affected zone (TMAZ) after FSW, with a decrease in the residual austenite and an increase in the degree of grain refinement. Saeid et al. [26] investigated the recrystallization behavior of different phases of duplex stainless steel during FSW. The results indicated that ferrite underwent a continuous dynamic recrystallization (CDRX), while a static recrystallization with CDRX may occur for austenite. Not long ago, Bagheri et al. [27] proposed a new welding technique called friction stir vibration brazing (FSVB) and successfully welded mild steel sheets using Sn–Pb brazing material. The results showed that FSVB is conducive to improving the quality of weld seam and grain refinement.

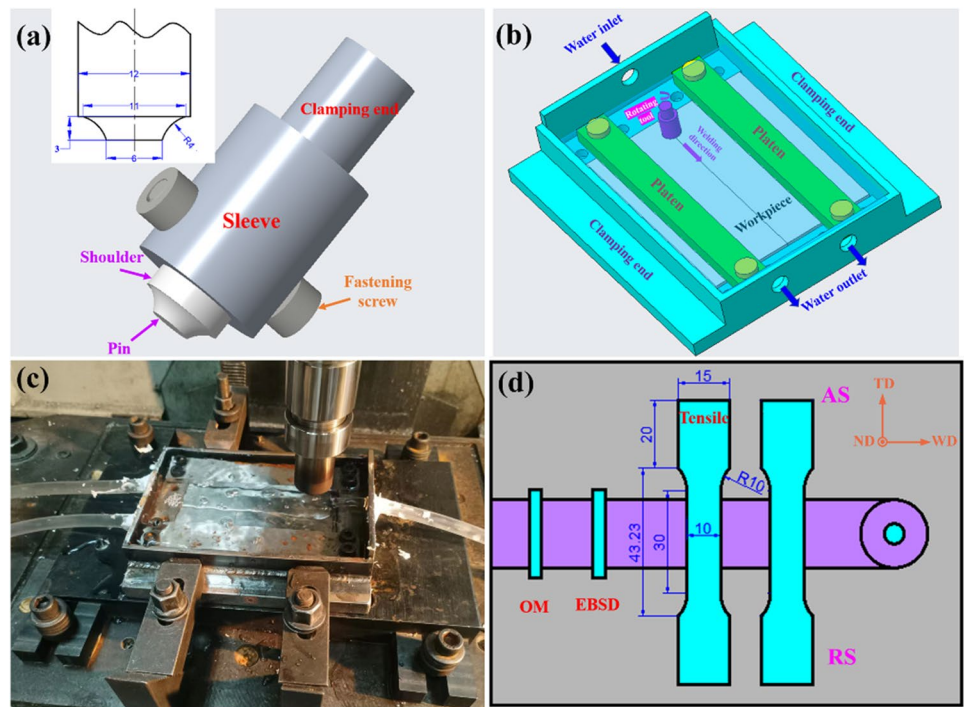
Nevertheless, there are few studies on the FSW of galvanized steel. Moreover, there is still a lack of in-depth research on the impact of the cooling rate on the FSW of galvanized steel. Considering the engineering value of galvanized steel, the study focused on the preparation of high-performance joints of galvanized steel by FSW and investigated the correlation between the microstructure evolution and mechanical behavior of joints at different cooling rates.

2 Materials and methods

2.1 Materials and FSW experiment

The BM is the hot dip galvanized steel (DX51D) with dimensions of 140 mm × 60 mm × 3 mm and its chemical composition includes 0.07 C, 0.32 Mn, 0.04 P, 0.02 S, 0.015 Si, 0.3 Ti, and Bal. Fe (wt.%). After a series of pre-experiments, the FSW experiments were performed, while maintaining the constant rotational (800 rpm) and transversal speeds (50 mm/min). The rotation tool maintained a tilt angle of 2° and an axial shoulder tie in depth of 0.3 mm during welding. A combined rotary tool was designed, as shown in Fig. 1(a). Unlike low melting point metals, steel will maintain considerable flow stress during FSW, which tends to lead to high

Fig. 1 **a** Assembly drawing and dimensional details of the rotary tool, **b** schematics of FSW and cooling system, **c** real picture of welding process, and **d** illustrate position and size of the measured specimen (unit: mm)



contact stress and tool wear [28]. Therefore, the welding tool made of W–Re and the clamping part made of H13 steel were designed to be assembled as two separate parts. The welding tool with a shoulder diameter of 12 mm comes with a concave conical pin 2.5 mm in length, which has a root diameter of 11 mm and a base diameter of 6 mm. This large-diameter concave conical pin not only enhances the plastic flow of the material but also helps to reduce wear and tear to extend the life of the tool [29].

A set of tooling was designed to vary the cooling rate of the weld, as shown in Fig. 1(b). The flowing room temperature water (20 °C) and hot water (80 °C) were introduced to ensure that the temperature around the welded workpiece is always constant during the cooling process. The height difference between the inlet and outlet holes is 50 mm. The inlet rate is controlled by adjusting the frequency of the motor, and the outlet rate is controlled by adjusting the number of outlet holes and the diameter of the water pipe. The flowing water was always guaranteed to submerge the workpiece surface during the experiment and the depth of the water is about 40 mm relative to the surface of the material to be processed. A thermocouple is used to check the water temperature to ensure that the water temperature is constant during the welding process. It is simple to understand that flowing water at 20 °C quickly removes the welding heat and enables fast cooling friction stir welding (FCFSW) of galvanized steel. Correspondingly, galvanized steel under a flowing water stream at 80 °C undergoes slow cooling stir friction welding (SCFSW). The actual scene of the welding process is shown in Fig. 1(c).

2.2 Microstructure characterization and mechanical property

The samples perpendicular to the welding direction were prepared to analyze the microstructure of welding zones, as revealed in Fig. 1(d). The normal, transverse, and welding directions were denoted as ND, TD, and WD, respectively. The optical microscope (OM: OLYMPUS GX51), electron backscattered diffraction (EBSD: Zeiss sigma 300), scanning electron microscope (SEM: FIB, Volumescope 2), Energy-Dispersive Spectrometer (EDS: Bruker, quantax-400) were used to characterize the microstructure, elements, and phases of the weld. The samples for OM were ground, polished, and etched for 15 s in an alcoholic nitric acid solution with a concentration of 4%. The samples with $8 \times 8 \times 3 \text{ mm}^3$ for EBSD were mechanically ground and mechanically polished, then electrolytically polished in the cross section with a solution of 10% perchloric acid and 90% ethanol at 25 V and 25 °C. The data was processed by Channel 5 software. In addition, low-angle grain boundaries (LAGBs) are defined as the GBs with a misorientation angle between 2 and 15°, and high-angle GBs (HAGBs) refer to the GBs with a misorientation angle above 15°.

Room temperature tensile tests were performed using an INSTRON 5965 testing machine with a stretching rate of 5 mm/min. Meanwhile, three tensile specimens of the joint were made along the TD to guarantee accuracy. Fracture topography and fracture characteristics were analyzed by using SEM. Figure 1(d) illustrates the shape and size of the tensile specimen.

3 Results and discussion

3.1 Macroscopic morphology

Macroscopic defects usually lead to internal defects in welds, so macroscopic morphology can be used as a standard for evaluating weld quality. Figure 2 (a) and (b) show the surface morphology after SCFSW and FCFSW, respectively. In both cases, no grooves or discontinuous defects were found on the surface. The difference is that the surface of the SCFSW joint exhibits a rougher annular structure as well as more flash. In addition, no excessive oxidation zone of the galvanized layer was observed on the surface of the FCFSW joint near the edge of the SZ compared to the SCFSW. This indicates that fast cooling significantly reduces the harsh effects of welding thermal cycling on the weld, which is because the flow ability of the plasticized metal diminishes with the reduction of heat input [30]. Mabuwa et al. [29] reported that flowing water has a strong cooling effect during the FSP process because the high specific heat capacity enables flowing water to acquire a high capacity for heat absorption and dissipation. This law was also demonstrated experimentally and through numerical simulations by Bagheri et al. [22, 27]. It is worth noting that the cooling efficiency of flowing water at 80 °C is greatly reduced compared to room temperature water although the cooling medium of this work is flowing water. Therefore, special attention needs to be paid to the cooling rate of the welding

environment although FSW can help to solve the metallurgical problems caused by fusion welding for the practical application of galvanized steel. Increasing the cooling rate can further prevent damage to the galvanized layer.

Figure 2 (c) and (d) are the cross sections of the two joints. The basin-shaped SZ can be clearly distinguished. The SZ is similar in shape to the rotary tool and a more pronounced onion ring structure is observed in the SCFSW joint. In addition, no defects are found in the two cross sections, which indicates that the selected process parameters are reasonable. According to Abbasi et al. [21], water-cooling will lead to an increase in the viscosity and the strain of the material rate within the SZ, which results in a greater influence of the welding tool on the material.

3.2 Microstructural analysis

3.2.1 Microstructural evolution

Although the macroscopic forming is good, the mechanical properties of materials are usually determined by the microstructure, so it is necessary to understand the evolution law of the microstructure before analyzing the mechanical properties. Combined with the F-Fe₃C phase diagram, the microstructure of the BM at different magnifications is made of predominantly white ferrite (F) and a small amount of black pearlite (P), as exhibited in Fig. 3(a), (b). The average grain size (AGS) is about 7.9 μm and there are some visible coarse grain areas (blue oval) and some fine grain areas (pink oval). The white F is irregular in shape and there are some black pearlites with larger sizes. The microstructures of the TMAZ + HAZ of the SCFSW and FCFSW joints (areas A and B in Fig. 2) are shown in Fig. 3(c), (d) and the microstructures of SZ are shown in Fig. 3(e), (f). Acicular F, which is produced by nucleation of inclusions during high-temperature cooling, was found in the TMAZ + HAZ and SZ of SCFSW [31], but not in TMAZ + HAZ and SZ of FCFSW. In addition, the FCFSW specimens had a narrower TMAZ + HAZ (AGS ≈ 4.4 μm) and higher grain refinement in the SZ than SCFSW (AGS ≈ 6.8 μm).

Overall, the microstructure of SCFSW shows acicular F, polygonal F, and P, while the weld is characterized by equiaxed F and diffuse P at fast cooling rates. Their morphology at higher multiples is shown in Fig. 4. Korkmaz et al. also found the presence of acicular F in TMAZ during the preparation of FSW joints of mild steel [31]. In the work, this phenomenon disappeared after accelerating the cooling rate, which can be explained by the temperature field. The temperature of FSW in steel under room temperature water cooling tends to be lower than the phase transition temperature, so F will undergo direct DRX without a phase transition, eventually forming fine equiaxed grains.

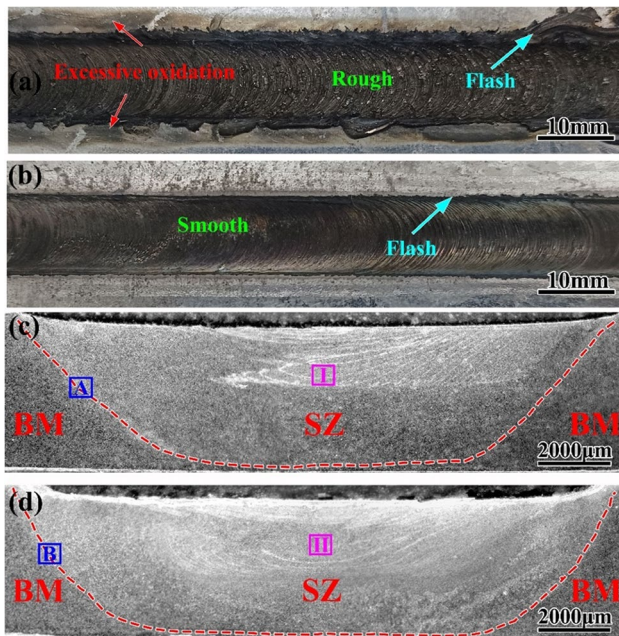


Fig. 2 a–d The surface and cross-sectional views after SCFSW and FCFSW, respectively

Fig. 3 Optical morphology of microstructures of different samples. **a** and **b** BM. **c** and **d** Areas A and B in Fig. 2. **e** and **f** SZ of SCFSW and FCFSW

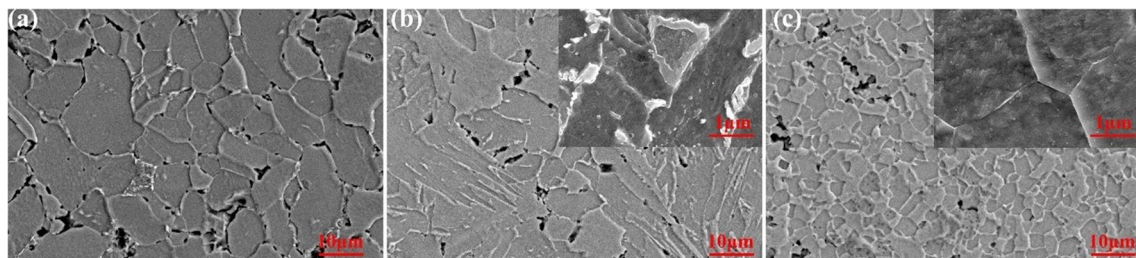
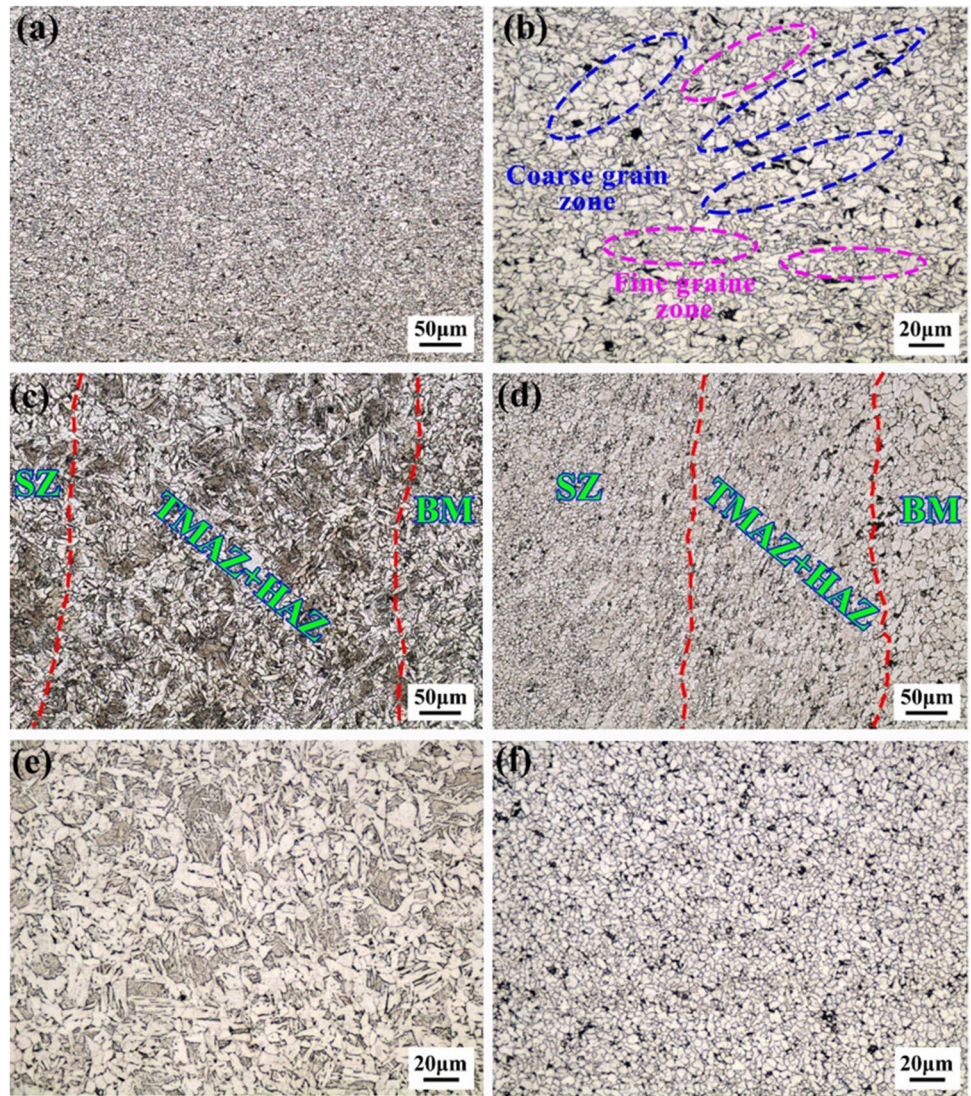


Fig. 4 SEM results of BM and SZ of different cooling rates: **a** BM, **b** SCFSW, and **c** FCFSW

The material near the rotating tool can usually be divided into a crush zone (CZ) and a flow zone (FZ) during FSW [32]. The material in the FZ follows the tool and undergoes intense DRX, which is known as the friction stirring effect. The material in the CZ moves away from the rotating tool and does not flow but is compressed at high temperatures.

As the tool moves towards the weld, the material in the CZ is rapidly heated, deformed, and recrystallized when it comes into contact with the hot material in the FZ [32]. During FSW, the material in the FZ softens significantly at high temperatures. The material in the HAZ usually retains considerable strength for engineering alloys such as galvanized

steel, so that the weld cross-sectional area is only slightly larger than the diameter of the pin. In addition, when the CZ collides with the hot FZ, the deformed grains are heated and undergo more plastic deformation, evolving into fine equiaxed crystals mainly through DRX. The grain size after DRX is usually negatively correlated with the Zener-Hollomon parameter (Z). The strain rate ($\dot{\epsilon}$) and the ambient temperature (T) are commonly used to describe Z as follows [19, 21]:

$$Z = \dot{\epsilon} \exp\left(\frac{Q}{RT}\right) \quad (1)$$

where Q and R stand for the activation energy and constant, respectively. Therefore, the temperature around the weld is low and the grain size in the SZ is significantly reduced during FCFSW. As reported by Bagheri et al. [22], slow cooling rates tend to lead to large grain sizes, while higher DRX occurs and recrystallized grains fail to grow.

3.2.2 The mechanism of dynamic recrystallization

Although OM can reflect grain size and morphology, it is difficult to analyze the crystallographic characteristics of the weld. Therefore, EBSD along the TD-ND plane analysis was performed to more clearly elucidate the mechanism

of microstructure evolution under different cooling rates, as shown in Fig. 5. Channel 5 software was used to calculate the equivalent circle diameter of each grain to measure the grain size. The AGS is the average value of the equivalent circle diameter of all grains. The calculation formula is as follows:

$$d_{\text{AGS}} = D/N \quad (2)$$

where D is the sum of the sizes of all grains being counted and N is the total number of grains to be counted. The initial microstructure is a vital factor in determining the properties of metals and alloys. It can be seen from Fig. 5(a)–(d) that the initial microstructure suffered from hot rolling was inhomogeneous and consisted of elongated grains and some equiaxed grains. The AGS is about 7.9 μm . The GB misorientation distribution confirms that the HAGBs are as high as 90.4%, which demonstrate that BM undergoes a long period of DRX during hot rolling.

Figure 5(e)–(l) show the EBSD results of SZ in FCFSW and SCFSW joints. Compared with BM, the grains of the FCFSW sample are refined while the grains of SZ are coarsened in the case of slow cooling (Fig. 5 (e) and (i)). The AGS of the SCFSW joint is about 6.2 μm but some grains are significantly larger than BM. The AGS of the FCFSW sample was about 2.3 μm , which is consistent with the results in

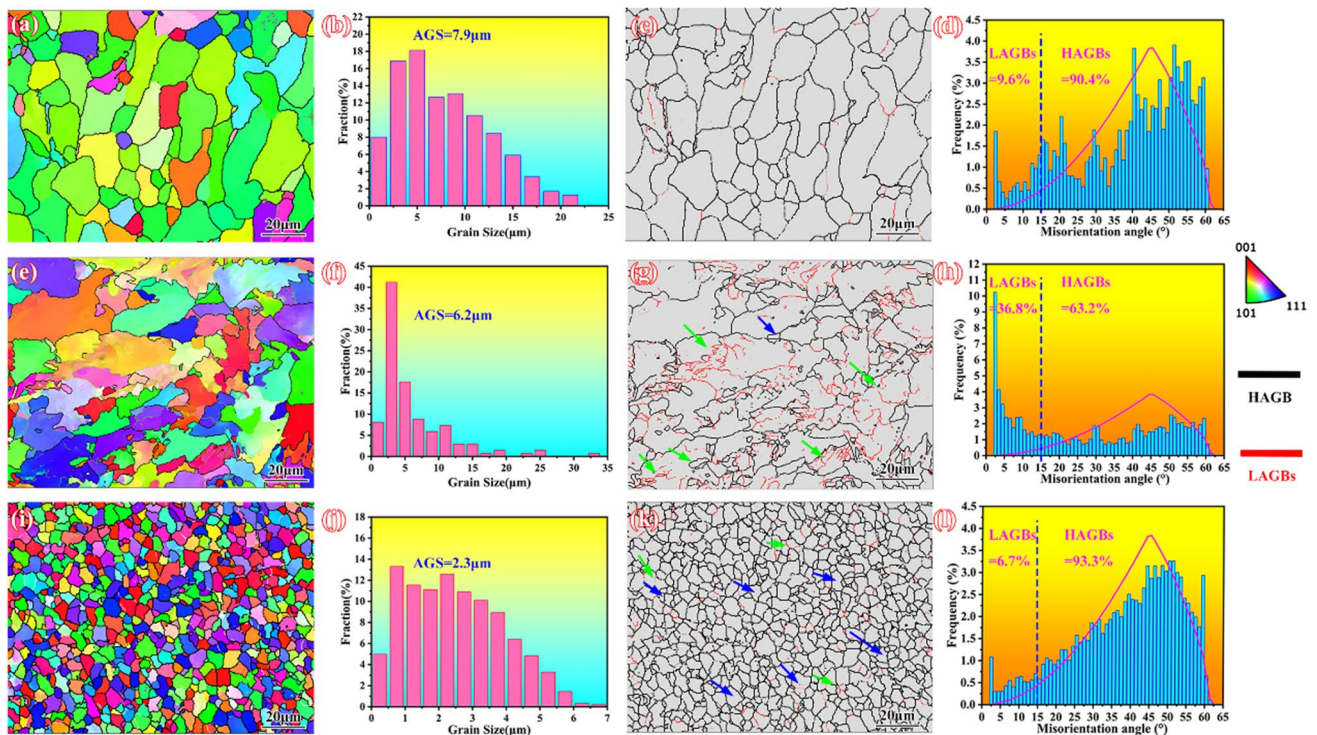


Fig. 5 IPF map, grain size histogram, GBs, and misorientation angle distribution under cooling rates corresponding to BM, areas I and II in Fig. 3. a–d BM, e–h SCFSW, and i–l FCFSW

Fig. 3. As discussed by Cao et al. [24], the thermal field was very sensitive to the submergence conditions, which affects not only the peak temperature, but also the time taken for the material to exceed a certain temperature. Therefore, lower peak temperature and shorter high-temperature residence time lead to more grain refinement.

Interestingly, the results for GBs show significant differences in the microstructure evolution mechanism in the weld of galvanized steel. The fractions of HAGBs for SCFSW and FCFSW joints are 63.2% and 93.3%, respectively, as shown in Fig. 5 (g),(h) and (k), (l), which indicate that a higher cooling rate favors the elimination of LAGBs. During FSW, the material within the flow zone underwent DRX. Dislocations would be rearranged and sub-grains that are often considered as LAGBs were formed. Subsequently, the rotation of the sub-GBs led to an increase in the misorientation angle, and the sub-GBs gradually evolved into HAGBs. The initial sub-grains were small due to the lower temperature, and fine grains were formed as the sub-grains evolved toward the main grains, which resulted in a higher proportion of HAGBs [21].

Differences in GBs are often due to different DRX mechanisms. The continuous dynamic recrystallization (CDRX) grains are shown by the green arrows in Fig. 5 (g) and (k). It is characterized by an increasing misorientation angle and a small migration of GBs with the accumulation and rotation of sub-GBs [33]. This phenomenon was particularly evident in the SCFSW sample. The fine equiaxed dislocation-free grains shown by blue arrows in Fig. 5 (g) and (k) are considered discontinuous dynamic recrystallization (DDRX) nuclei. It is characterized by the extension from the original GB to the region where recrystallization did not occur [34, 35]. Based on the above analysis, it can be concluded that the DRX mechanism is controlled by both

DDRX and CDRX during the FSW of galvanized steel. As can be seen in Fig. 5(e), the dislocation-free grains generated by DDRX are finer and surrounded by coarse grains. The reason for this is that the first layer of nuclei in the initial stage of DDRX tends to form a typical chain-like structure [34]. In addition, the proportion of LAGBs is as high as 36.8% (Fig. 5(h)), which indicates that a large number of sub-structures were retained just at the beginning of CDRX (Fig. 5(g)). In contrast, the SZ of FCFSW is dominated by fine dislocation-free equiaxed grains (Fig. 5(i)) and the percentage of LAGBs is only 6.7% (Fig. 5(l)), which indicates that DDRX is dominant and completed.

An important factor affecting the DRX mechanism is the stacking fault energy (SFE) during FSW [36]. On the one hand, dynamic recovery (DRV) is easier for metals with high SFE. Therefore, dislocation slipping and climbing during deformation is faster and it is easier to rearrange into sub-GBs; thus, CDRX is an effective mechanism for the formation of HAGBs, as shown in Fig. 6(a). On the other hand, dislocation slipping and climbing are difficult and accumulate inside the grains for low SFE materials. When a critical strain is reached, the high dislocation density difference between adjacent grains will provide the driving force for DDRX-shaped cores [36–38], as shown in Fig. 6(b). It is well known that ferritic steel is a high SFE material. Theoretically, CDRX is the main mechanism of DRX in FSW. CDRX is the main mechanism for the SCFSW sample, but DDRX is the main mechanism for the FCFSW sample. Therefore, it is necessary to consider the effect of the cooling rate. The approximate formula for the peak temperature during FSW is [39]

$$\frac{T_p}{T_m} = K \left(\frac{\omega^2}{10^4 v} \right)^\alpha \quad (3)$$

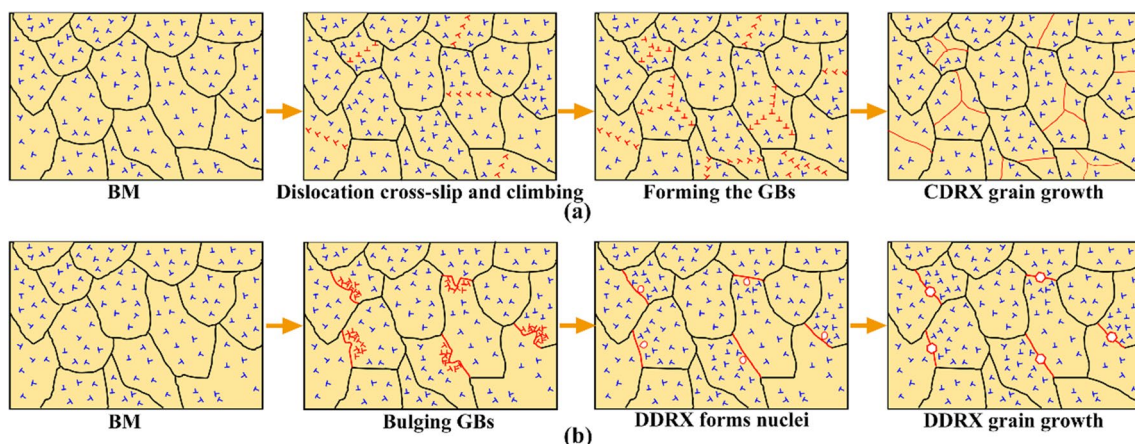


Fig. 6 a The mechanism diagram of CDRX and b the mechanism diagram of DDRX

where T_p is the peak temperature ($^{\circ}\text{C}$) of the weld, T_m is the melting point ($^{\circ}\text{C}$) of the metal, ω is the rotation speed of the tool, v is the welding speed, and α and K are the constants. Since the welding parameters are consistent, the peak weld temperature is theoretically approximated. However, the peak temperature may only exist for a moment and then drop rapidly under fast cooling conditions, while the high temperature will stay for a longer time under a slow cooling environment. Higher temperatures will lead to higher SFE [40]. As a result, the decrease in peak temperature and high-temperature residence time results in a lower SFE and a more difficult CDRX as the cooling rate increases.

The temperature of steel during FSW/P is much higher than the temperature during heat deformation, as demonstrated by several studies [33, 41–43]. Excessive temperature promotes DRV, during which a large number of dislocations slip and climb and form large misorientation angles that may subsequently turn into grain boundaries. Therefore, DRV is a major cause of CDRX. In addition, numerous studies [44, 45] have shown that CDRX is the main evolutionary mechanism of SZ for the conventional FSP/W of steel. However, Hajian et al. showed that temperature drop prompted the disappearance of CDRX and the dominance of DDRX [36], which seems to echo the work.

Furthermore, the experimental phenomenon can also be explained by the strain rate. It can be expressed by the following equation [46, 47]:

$$\dot{\epsilon} = AF(\sigma)\exp[-Q/RT] \quad (4)$$

$$F(\sigma) = \begin{cases} \sigma^N \\ \exp(\beta\sigma) \\ \sinh(\alpha\sigma)^n \end{cases} \quad (5)$$

where $\dot{\epsilon}$ is the strain rate (s^{-1}); A , α , β , N , and n are the material constants and $\alpha = \beta/N$; Q is the apparent activation energy for deformation; R is the gas constant ($8.3145 \text{ J}\cdot\text{mol}^{-1}\cdot\text{K}^{-1}$); T is the temperature (K); and σ is the true stress (MPa). It is clear from this equation that strain rate is positively correlated with temperature. It can also be understood that high temperatures cause the material to soften, making it more susceptible to deformation and thus producing greater strain per unit of time. A decrease in the strain rate will lead to a prolongation of the deformation time, which will increase the dislocation density. As a result, the critical strain for DRX decreases, increasing the probability of DRX. Therefore, the critical stress of DRX during the deformation of steel shows a positive strain rate sensitivity [48]. In addition, the shear stresses and axial forces are much higher during FCFSW compared to high-temperature FSW [22, 49, 50], which provide the driving force for DRX. The above discussion reveals the complexity of DRX during the FSW. We believe that the microstructural evolution in SZ results from the competition between CDRX and DDRX. They are sensitive to temperature and strain.

Grain orientation spread (GOS) allows analysis of the recrystallization process under different conditions, as shown in Fig. 7. The microstructure of BM is dominated by recrystallized grains (64.8%) and has almost no deformed grains. The microstructure of the joints under

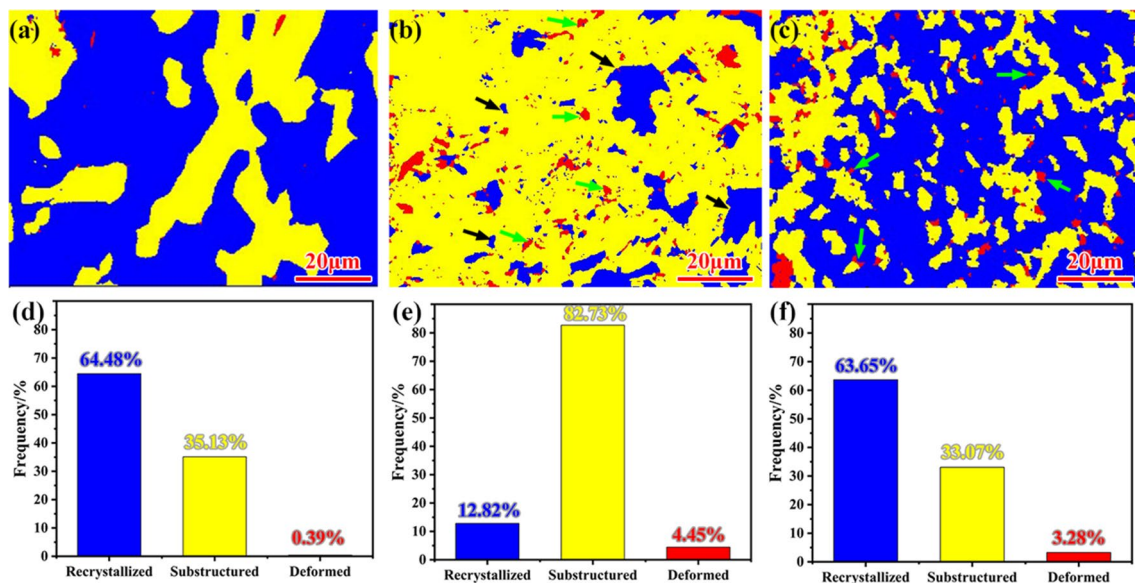


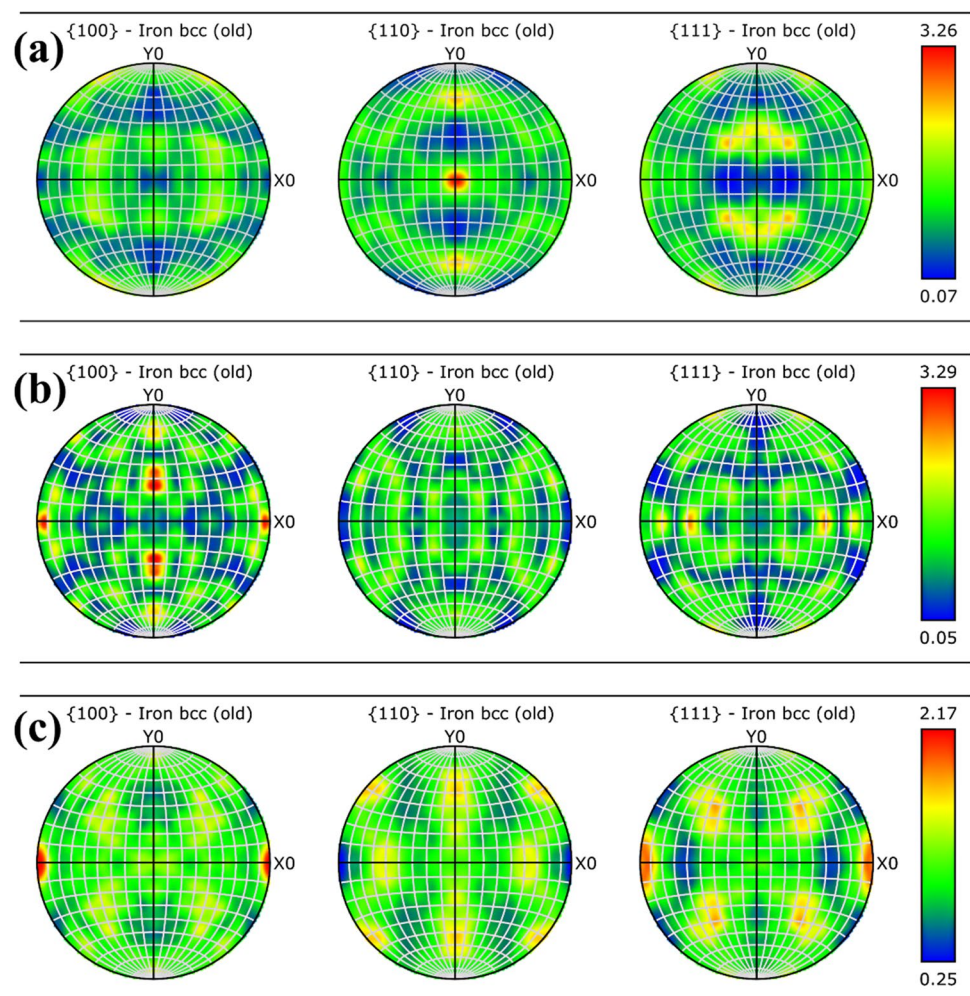
Fig. 7 Recrystallized grain distribution diagram and proportion diagram in different regions (red: deformed grains; yellow: sub-structured grains; blue: recrystallized grain): **a** and **d** BM, **b** and **e** SCFSW-SZ, and **c** and **f** FCFSW-SZ

slow cooling has sub-structured grains up to 82.73% and a small number of deformed grains (4.45%). The arrows in Fig. 7(b) mark the recrystallized grains (black arrows) and deformed grains (green arrows). On the one hand, the presence of sub-structured grains around both recrystallized and deformed grains suggests that the sub-structured grains are formed by consuming deformed grains, and then the internal dislocations of these grains are rearranged to form sub-GBs, followed by the formation of recrystallized grains (Fig. 6(a)). On the other hand, there are large differences in the size and shape of recrystallized grains except for the small percentage, which indicates that CDRX is at the beginning stage, generating a large number of recrystallized nuclei, and the completed recrystallized grains grew rapidly at high temperatures. In fact, the long high-temperature duration prolonged the DRV and promoted the development of CDRX due to the decrease in cooling rate [36]. This is consistent with the previous analysis. The recrystallized grains in the joint under rapid cooling conditions reach 63.65%, which is comparable to BM, but a small number of deformed grains (3.28%) is present.

The green arrow shows the deformed grains surrounded by recrystallized grains. In other words, the recrystallized grains are grown by direct consumption of the deformed grains, and dislocations are annihilated by DDRX. The recrystallized grains are retained at room temperature due to faster cooling.

Some significant differences in the final texture can be observed in SZ due to the different DRX mechanisms, as shown in Fig. 8. The maximum texture strength of BM reaches 3.26. The texture strength with slow cooling reaches as high as 3.29, which means that the anisotropy of the weld is similar to that of BM [51]. Upon rapid cooling, the texture weakens to 2.17, which is beneficial for improving the anisotropy of mechanical properties. We simply attribute the reasons for the texture changes to different DRX mechanisms. According to Sabooni et al. [44], DRV and CDRX are prone to forming shear deformation textures, while grain nucleation and growth during DDRX often lead to the formation of cubic textures. As this was not the focus of this study, further in-depth discussion is not necessary. However, improved texture could be an advantage of FCFSW.

Fig. 8 **a** The pole figure of BM. **b** and **c** The pole figures of SZ under slow- and fast-cooled environments



3.2.3 Dislocation and phase analysis

In addition to crystallographic information, dislocations and phase distributions are also important components of microstructure evolution. Therefore, this section will analyze some simple sub-structure and phase information by EBSD.

For deformed materials, dislocation accumulation will inevitably occur near grain boundaries due to the proliferation and slip of dislocations, leading to an increase in the density of geometrically necessary dislocations (GND) near grain boundaries. These are low-strain compatibility regions between deformed grains, where lattice rotation occurs near the boundary to accommodate the necessary strain in each grain. Formula (6) describes the positive correlation between dislocation density and strain [52]:

$$\alpha_{ij} = e_{ikl}(\epsilon_{jl,k}^e + g_{jl,k}) \quad (6)$$

where α_{ij} is the dislocation density tensor, e_{ikl} is the permutation tensor, $\epsilon_{jl,k}^e$ is the gradient of the elastic strain, and $g_{jl,k}$ is the lattice curvature as measured by EBSD. Kernel average misorientation (KAM) is commonly used to characterize the local strain distribution of crystal materials. Therefore, GND density can be analyzed by observing the KAM map [53].

Figure 9(a)–(c) show the KAM maps of the BM as well as the joints at different cooling rates. The average KAM value of the BM is only 0.3° (Fig. 9(a)), which is the result of the occurrence of sufficient DRX within the BM. According to Eq. (6), the dislocation density increased significantly due to the drastic plastic deformation of the microstructure

grains of SZ during the FSW. As analyzed earlier, the SZ of SCFSW has a high strain because of the high temperature and severe softening of the material (Eq. (5)). A linear relationship between dislocation density and strain has also been reported by Bagheri et al. [27]. Dislocation density increases rapidly with strain. Therefore, the weld under slow cooling has a KAM value as high as 0.5° and a large number of high-strain zones (Fig. 9(b)). In contrast, the samples of fast cooling obtained an average KAM value (0.4°) higher than that of the BM and a very uniform KAM distribution (Fig. 9(c)), which symbolizes more uniform dislocations and strains. It can be inferred that appropriately increasing the cooling rate may be an effective means to improve the dislocation uniformity.

The distribution characteristics of the second phase are crucial for the mechanical properties of the material. Figure 9(d)–(f) show the phase maps of BM and SZ. The percentage of Fe_3C in BM is about 0.5% (Fig. 9(d)), which increases to 1.4% at a slow cooling rate (Fig. 9(e)), but some enriched areas and large second-phase particles can be observed. It is easy to see that these enriched areas and large-size particles are located in the high-strain region. The reasons can be attributed to the following: (1) the long high-temperature residence time provides conditions for the anomalous growth of the second phase; (2) some high-strain regions may become favorable locations for DRX nucleation [54]. In contrast, the second phase diffusely and uniformly precipitated in the SZ of the FCSW. It can be easily understood that the uniform KAM and the diffuse precipitates are effective means to synergistically improve the strength-ductility of joints [24]. The strengthening induced by the

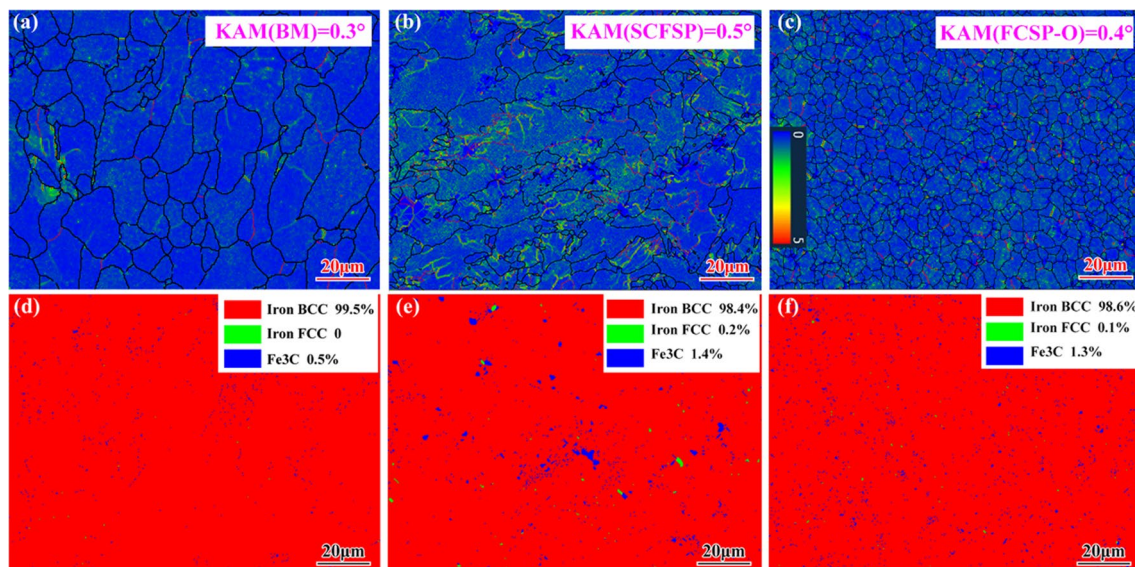


Fig. 9 a–c The KAM maps of BM, SCFSW-SZ, and FCFSW-SZ respectively. d–f The phase maps of BM, SCFSW-SZ, and FCFSW-SZ respectively

precipitates depends on the size of the precipitation and the intergranular distance [21]. By increasing the cooling rate, the precipitates in FCFSW samples are smaller and more diffuse, which will contribute to the improvement of the mechanical properties.

In summary, FCFSW shows significant advantages over SCFSW, which has provided more than enough evidence to analyze the mechanical property differences. Therefore, more detailed sub-structural and phase information that may need to be characterized by transmission electron microscopy is not essential in this work.

3.3 Mechanical behavior

The tensile properties of BM and SZs manufactured in different cooling environments are shown in Fig. 10. Figure 10(a) shows the stress–strain curve and fracture location. The upper yield strength (UYS), lower yield strength (LYS), ultimate tensile strength (UTS), and elongation (ER) of the tensile specimens are shown in Fig. 10(b). The BM specimens failed near the middle due to the similar microstructure state within the scale, which is a typical fracture location for rolled samples [24, 55, 56]. All welding specimens failed in the BM zone with necking at the fracture, which implies that the specimens had significant plastic deformation before the fracture. The study by Wang et al. [57] demonstrated that the tightening and fracture of the specimens of FSW occurred mainly in the BM rather than the weld during tension. The main reason for this is that the refinement of the microstructure and the precipitates will lead to inconsistencies in the ability to hinder dislocation movement at different locations during stretching. As a result, dislocations have difficulty slipping in the SZ, leading to tightening and fracture of the “softer” BM. It is worth mentioning that some studies have shown that the HAZ is often used as a fracture location for the weld [58, 59]. This can be explained by the characteristics of the FSW process, which has a much lower temperature than other welding processes. In particular, the coolant used in this work kept the HAZ from softening and thus from becoming a fracture point.

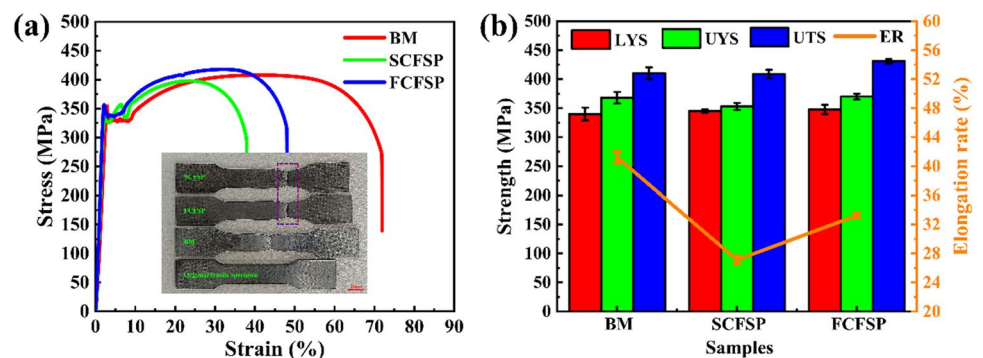
The stress–strain curve (Fig. 10(a)) shows that the strain at the break of the BM specimen is greater than that of the FSW specimen, which is due to the fact that the deformation is mainly contributed by the BM part of the tensile specimen [57]. This suggests that FSW weakens the plasticity of the weld to some extent. As shown in Fig. 10(b), the elongation rate (ER) of the specimens with FSW is reduced compared to BM (41.23%). The reduction in ER is more significant for SCFSW samples (27.12%) than for FCFSW samples (33.24%). At the same time, the tensile strength of the FSW specimens depends on the portion of the BM because HAZ is not softened. Therefore, the tensile strength of the FSW specimen can be greater than that of the BM specimen, as shown in Fig. 10(b). The UTS of the SCFSW specimen reaches 409 MPa which is comparable to that of the BM (410 MPa) and the UTS of the FCFSW specimen up to 431 MPa has surpassed that of the BM. Interestingly, the UYS (353 MPa) of the SCFSW specimens are slightly lower than those of the BM (UYS_{BM} = 368 MPa), while both the UYS (370 MPa) and LYS (348 MPa) of the FCFSW specimens surpass the BM.

Combined with the previous microstructure evolution analysis, we attribute the above phenomena to the combined results of grain boundary strengthening, dislocation strengthening, and precipitation strengthening. Firstly, according to the Hall-Pitch relationship [60], the reduction of grain size will significantly increase strength. The Hall-Pitch relationship is as follows:

$$\sigma_s = \sigma_0 + kd^{-1/2} \tag{7}$$

where σ_s refers to the yield strength, d is the grain size, and σ_s and k are the material-dependent constants. The GB area will increase as the grain size decreases. The GBs hinder the dislocation movement, which will lead to an increase in strength. In addition, the increase in dislocation density further limits dislocation slip. Last but not least, the homogeneous distribution of fine second-phase particles increases the “pinning” effect of the dislocations by the “Cottrell atmosphere” [61–63]. The specimens under fast cooling have

Fig. 10 Mechanical properties of BM, SCFSW, and FCFSW along the TD directions. **a** Engineering stress–strain curves and fracture location and **b** average LYS, UYS, UTS, and ER statistics of the corresponding stretched samples



considerable advantages in all aspects, which is a decisive factor for their strength to exceed that of BM. On the contrary, the grain refinement effect of SZ under slow cooling is not satisfactory and the large number of stress concentration zones and inhomogeneous second-phase distribution also limit the strength and plasticity of the material.

Figure 11 shows the SEM images of tensile fracture surfaces. Ductile fractures with significant tightening can be observed on the fracture surfaces of all specimens and all fractures show fibrous surfaces without shear lips and radial zones (Fig. 11(a)). Usually, the fibrous zone is the origin of the fracture source, where the cracks are nucleated, extended, and aggregated [59]. This is logical since all specimens fractured at the BM (Fig. 10). The high-magnification morphology of the fracture of the BM specimens exhibited approximately equiaxed coarse and fine tough nests (Fig. 11(b)), which indicates good ductility of the BM. The fracture tough nest size and depth of the specimens after FSW were reduced as a result of the reduced ductility (Fig. 11(c, d)).

There are many theories to explain the change in ductility. Ashrafi et al. [64] showed that the work-hardening rate of metals increases with increasing grain size, which implies that smaller grains are beneficial in slowing down the work-hardening rate and contributing to ductility. Hajian et al. [36] attributed the decrease in plasticity after FSW to the decrease in grain size which reduces the effective slip distance of dislocations and accelerates the buildup of dislocations on GBs. In other words, the strain-hardening rate will increase when the slip is hindered. Since the plastic deformation process is always accompanied by the proliferation

and slip of dislocations, the ability of the grains to adapt to the increase in the dislocation density is an important influence on the plasticity of the material. The finer the grain, the smaller the ability of the grain to adapt to the increase in dislocation density. Meanwhile, the coarse precipitation tends to lead to stress concentration, which will further reduce the ductility of SCFSW. Therefore, the results shown in Figs. 10 and 11 are reasonable.

Furthermore, the strains of the joints are not uniform at different locations during the tensile process, as shown in Fig. 12(a). The mobility of dislocations decreases as the grain size decreases, which results in less deformation of the material within the weld [27]. Therefore, the BM region outside the SZ is required to deform at a greater strain rate to match the constant global strain rate due to the lack of softening and the overall increase of strength in SZ, which manifests itself as an enhancement of the YS [65]. The material within the marked distance does not have a region where

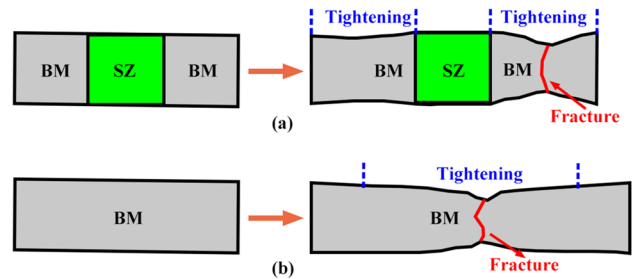
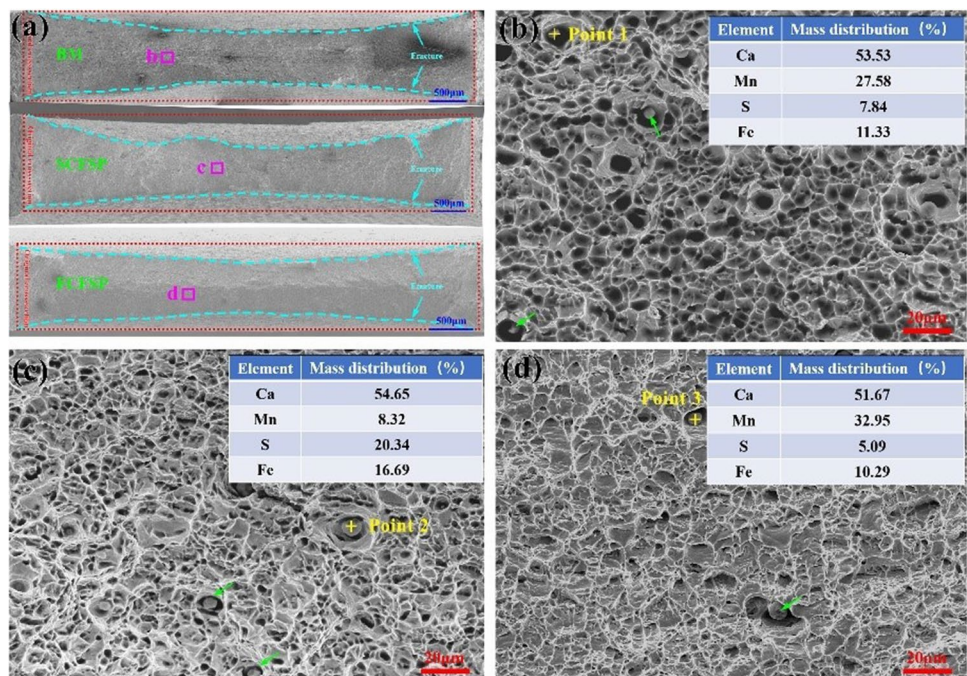


Fig. 12 Diagram of tightening mechanism of BM and FSW joint during stretching. a FSW joint and b BM

Fig. 11 SEM images of tensile fracture surfaces: a cross-section morphology after fracture, b BM, c SCFSW, and d FCFSW



the strain difference is too large for BM, so ductility is better (Fig. 12(b)). Moreover, some granular substances (indicated by the green arrow) can be found in the dimples of each specimen's fracture surface. EDS results show that these particles all have a high proportion of Ca. Ca may exist as an impurity element during the preparation of BM and play a negative role in the tensile process, leading to early fracture of the material. Therefore, it may be necessary to further regulate the process during the preparation of galvanized steel BM to reduce impurity elements.

4 Conclusion

The welded joints of galvanized steel were successfully fabricated by friction stir welding (FSW) with different cooling rates. The following conclusions can be drawn:

- (1) Cooling rate affects the recrystallization mechanism of galvanized steel. The microstructure evolution mechanism in the stirring zone is mainly discontinuous dynamic recrystallization at a fast cooling rate, while the mechanism is mainly continuous dynamic recrystallization at a slow cooling rate.
- (2) Rapid cooling is more conducive to microstructure refinement, weakening of the weave structure, and diffuse precipitation of Fe_3C .
- (3) FSW easily leads to the loss of plasticity of the joint, but accelerating the cooling rate is beneficial to alleviate this loss. Therefore, FSW joints with fast cooling gained strength beyond that of the base material while maintaining good ductility.

Acknowledgements We thank the Technology Research Institute of Nanjing Chenguang Group Co., Ltd. for its great help and the Analysis and Test Center of Nanjing University of Aeronautics and Astronautics for providing the SEM analysis technology.

Author contribution Tao Sun: investigation, conceptualization, writing—original draft, writing—review and editing. Jianhui Wu: investigation, formal analysis. Zhihui Yang: investigation. Wang Ge: formal analysis. Guoqiang Huang: investigation, formal analysis. Yifu Shen: supervision, funding acquisition, writing—review and editing.

Funding Financial support was provided by the National Natural Science Foundation of China (Grant No. 52275217).

Data availability Data will be made available on request.

Code availability Not applicable.

Declarations

Ethical approval Not applicable.

Consent to participate Not applicable.

Consent for publication Not applicable.

Conflict of interest The authors declare no competing interests.

References

1. Vaez S, Emadi R, Sadeghzade S, Salimijazi H, Kharaziha M (2022) Electrophoretic deposition of chitosan reinforced baghdadite ceramic nano-particles on the stainless steel 316L substrate to improve biological and physical characteristics. *Mater Chem Phys* 282:125991
2. Wu J, Cao FJ, Sun T, Huang GQ, Li MS, Hou WT, Piao ZY, Shen ZK, Shen YF (2023) Developing ultrafine-grained structure with balanced α/γ fraction via underwater friction stir processing enables enhanced wear and corrosion resistance of duplex stainless steel. *Surf Coatings Technol* 457:129295
3. Chen S, Zhang J, Wang D, Wang JX, Li RF (2019) Study on low axial load friction stir lap joining of 6061-T6 and zinc-coated steel. *Metall Mater Trans A Phys Metall Mater Sci* 50:4642–4651
4. Wan Z, Wang HP, Li J, Solomon J, Zhu YJ, Carlson B (2021) Novel measures for spatter prediction in laser welding of thin-gage zinc-coated steel. *Int J Heat Mass Transf* 167:120830
5. Zhang Y, Li Q, Xu L, Duan L (2015) A mechanistic study on the inhibition of zinc behavior during laser welding of galvanized steel. *J Manuf Sci Eng Trans ASME* 137:1–9
6. Xing B, Yan S, Zhou H, Chen H, Qin QH (2018) Qualitative and quantitative analysis of misaligned electrode degradation when welding galvanized steel. *Int J Adv Manuf Technol* 97:629–640
7. Zdravecká E, Slota J (2019) Mechanical and microstructural investigations of the laser welding of different zinc-coated steels. *Metals (Basel)* 9:1–13
8. Ma G, Yuan H, Yu L, He Y (2021) Monitoring of weld defects of visual sensing assisted GMAW process with galvanized steel. *Mater Manuf Process* 36:1178–1188
9. Cao FJ, Sun T, Hu JP, Hou WT, Huang GQ, Shen YF, Ma NS, Geng PH, Hu WY, Qu XY (2023) Enhanced mechanical and anti-corrosion properties in cryogenic friction stir processed duplex stainless steel. *Mater Des* 225:111492
10. Bagheri B, Sharifi F, Abbasi M, Abdollahzadeh A (2022) On the role of input welding parameters on the microstructure and mechanical properties of Al6061-T6 alloy during the friction stir welding: experimental and numerical investigation. *Proc Inst Mech Eng Part L J Mater Des Appl* 236:299–318
11. Adibeig MR, Vakili-Tahami F, Saeimi-Sadigh MA, Majnoun P, da Silva LFM (2021) Polyethylene FSSW/adhesive hybrid single strap joints: parametric optimization and FE simulation. *Int J Adhes Adhes* 111:102984
12. Adibeig MR, Hassanifard S, Vakili-Tahami F, Hattel JH (2018) Experimental investigation of tensile strength of friction stir welded butt joints on PMMA. *Mater Today Commun* 17:238–245
13. Schmidt HNB, Dickerson TL, Hattel JH (2006) Material flow in butt friction stir welds in AA2024-T3. *Acta Mater* 54:1199–1209
14. Schmidt H, Hattel J (2005) Modelling heat flow around tool probe in friction stir welding. *Sci Technol Weld Join* 10:176–186
15. Wang W, Han P, Peng P, Zhang T, Liu Q, Yuan SN, Huang LY, Yu HL, Qiao K, Wang KS (2020) Friction stir processing of magnesium alloys: a review. *Acta Metall Sin English Lett* 33:43–57
16. Abdollahzadeh A, Bagheri B, Abbasi M, Sharifi F, Mirsalehi SE, Moghaddam AO (2021) A modified version of friction stir welding process of aluminum alloys: analyzing the thermal treatment and wear behavior. *Proc Inst Mech Eng Part L J Mater Des Appl* 235:2291–2309

17. Abdollahzadeh A, Bagheri B, Abassi M, Kokabi AH, Moghaddam AO (2021) Comparison of the weldability of AA6061-T6 joint under different friction stir welding conditions. *J Mater Eng Perform* 30:1110–1127
18. Bagheri B, Abdollahzadeh A, Sharifi F, Abassi M, Moghaddam AO (2021) Recent development in friction stir processing of aluminum alloys: microstructure evolution, mechanical properties, wear and corrosion behaviors. *Proc Inst Mech Eng Part E J Process Mech Eng* 1:1–15
19. Abbasi M, Bagheri B, Sharifi F (2021) Simulation and experimental study of dynamic recrystallization process during friction stir vibration welding of magnesium alloys. *Trans Nonferrous Met Soc China (English Ed)* 31:2626–2650
20. Abbasi M, Bagheri B, Abdollahzadeh A, Moghaddam AO (2021) A different attempt to improve the formability of aluminum tailor welded blanks (TWB) produced by the FSW. *Int J Mater Form* 14:1189–1208
21. Abbasi M, Abdollahzadeh A, Bagheri B, Moghaddam AO, Sharifi F, Dadaei M (2021) Study on the effect of the welding environment on the dynamic recrystallization phenomenon and residual stresses during the friction stir welding process of aluminum alloy. *Proc Inst Mech Eng Part L J Mater Des Appl* 235:1809–1826
22. Bagheri B, Abbasi M, Abdolazadeh A, Kokabi AH (2020) Numerical analysis of cooling and joining speed effects on friction stir welding by smoothed particle hydrodynamics (SPH). *Arch Appl Mech* 90:2275–2296
23. Luo L, Yang BH, Quan QQ, Yang XR, Liu XY, Wang JZ (2022) Effect of rapid cooling on the microstructure and properties of fine-grained 7075 aluminium alloy under friction stir welding. *Mater Res Express* 9:056521
24. Cao F, Huang G, Hou W, Ni RY, Sun T, Hu JP, Shen YF, Gerlich AP (2022) Simultaneously enhanced strength-ductility synergy and corrosion resistance in submerged friction stir welded super duplex stainless steel joint via creating ultrafine microstructure. *J Mater Process Technol* 307:117660
25. Wang W, Zhang S, Qiao K, Wang KS, Peng P, Yuan SN, Chen SY, Zhang T, Wang Q, Liu T, Yang Q (2020) Microstructure and mechanical properties of friction stir welded joint of TRIP steel. *J Manuf Process* 56:623–634
26. Saeid T, Abdollah-zadeh A, Shibayanagi T, Ikeuchi K, Assadi H (2010) On the formation of grain structure during friction stir welding of duplex stainless steel. *Mater Sci Eng A* 527:6484–6488
27. Bagheri B, Abbasi M, Sharifi F, Abdollahzadeh A (2022) Different attempt to improve friction stir brazing: effect of mechanical vibration and rotational speed. *Met Mater Int* 28:2239–2251
28. Liu FC, Hovanski Y, Miles MP, Sorensen CD, Nelson TW (2018) A review of friction stir welding of steels: tool, material flow, microstructure, and properties. *J Mater Sci Technol* 34:39–57
29. Zhang HJ, Wang M, Zhu Z, Zhang X, Yu T, Wu ZQ (2018) Impact of shoulder concavity on non-tool-tilt friction stir welding of 5052 aluminum alloy. *Int J Adv Manuf Technol* 96:1497–1506
30. Hosseini M, Danesh Manesh H (2010) Immersed friction stir welding of ultrafine grained accumulative roll-bonded Al alloy. *Mater Des* 31:4786–4791
31. Korkmaz E, Meran C (2024) The examination of microstructural and mechanical properties of friction stir welded XPF800 steel. *Proc Inst Mech Eng Part C J Mech Eng Sci* 238:138–147
32. Wan L, Huang Y (2018) Friction stir welding of dissimilar aluminum alloys and steels: a review. *Int J Adv Manuf Technol* 99:1781–1811
33. Wang T, Zou Y, Matsuda K (2016) Micro-structure and micro-textural studies of friction stir welded AA6061-T6 subjected to different rotation speeds. *Mater Des* 90:13–21
34. Xi T, Yang C, Babar Shahzad M, Yang K (2015) Study of the processing map and hot deformation behavior of a Cu-bearing 317LN austenitic stainless steel. *Mater Des* 87:303–312
35. Cai Y, Xiang S, Tan Y (2022) Insight into the dynamic recrystallization behavior and microstructure evolution of MP159 superalloy during hot deformation. *Met Mater Int* 28:2381–2394
36. Hajian M, Abdollah-zadeh A, Rezaei-Nejad SS, Zhang X, Yu T, Wu ZQ (2015) Microstructure and mechanical properties of friction stir processed AISI 316L stainless steel. *Mater Des* 67:82–94
37. Sajadifar SV, Hosseinzadeh A, Richter J, Krochmal M, Wegener T, Bolender A, Heidarzadeh A, Niendorf T, Yapici GG (2022) On the friction stir processing of additive-manufactured 316L stainless steel. *Adv Eng Mater* 24:1–11
38. Chen YC, Fujii H, Tsumura T, Kitagawa Y, Nakata K, Ikeuchi K, Matsubayashi K, Michishita Y, Fujiya Y, Katoh J (2012) Banded structure and its distribution in friction stir processing of 316L austenitic stainless steel. *J Nucl Mater* 420:497–500
39. Mishra RS, Ma ZY (2005) Friction stir welding and processing. *Mater Sci Eng R Reports* 50:1–78
40. Neding B, Tian Y, Ko JYP, Hedström P (2022) Correlating temperature-dependent stacking fault energy and in-situ bulk deformation behavior for a metastable austenitic stainless steel. *Mater Sci Eng A* 832:142403
41. Dehghan-Manshadi A, Barnett MR, Hodgson PD (2008) Recrystallization in AISI 304 austenitic stainless steel during and after hot deformation. *Mater Sci Eng A* 485:664–672
42. Puli R, Janaki Ram GD (2012) Dynamic recrystallization in friction surfaced austenitic stainless steel coatings. *Mater Charact* 74:49–54
43. Belyakov A, Miura H, Sakai T (1998) Dynamic recrystallization under warm deformation of a 304 type austenitic stainless steel. *Mater Sci Eng A* 255:139–147
44. Sabooni S, Karimzadeh F, Enayati MH, Ngan AHW (2015) Friction-stir welding of ultrafine grained austenitic 304L stainless steel produced by martensitic thermomechanical processing. *Mater Des* 76:130–140
45. Jeon JJ, Mironov S, Sato YS, Kokawa H, Park SHC, Hirano S (2013) Grain structure development during friction stir welding of single-crystal austenitic stainless steel. *Metall Mater Trans A Phys Metall Mater Sci* 44:3157–3166
46. Zener C, Hollomon JH (1944) Effect of strain rate upon plastic flow of steel. *J Appl Phys* 15:22–32
47. Abedi HR, Zarei Hanzaki A, Liu Z, Xin R, Haghdadi N, Hodgson PD (2017) Continuous dynamic recrystallization in low density steel. *Mater Des* 114:55–64
48. Huang Y, Wang S, Xiao Z, Liu H (2017) Critical condition of dynamic recrystallization in 35CrMo steel. *Metals (Basel)* 7:1–13
49. Tahar M, Moustafa B, Mouloud A, Tawfiq C, Abdelkader Z, Mounir Z (2023) Experimental investigation and numerical analysis using Taguchi and ANOVA methods for underwater friction stir welding of aluminium alloy 2017 process improvement. *Int J Pres Ves Pip* 201:104879
50. Jain R, Pal SK, Singh SB (2016) A study on the variation of forces and temperature in a friction stir welding process: a finite element approach. *J Manuf Process* 23:278–286
51. Liu W, Yan Y, Ni R, Sun T, Wu SY, Shen YF (2021) Influence of preheating temperature on the friction stir welded ME20M magnesium alloy. *Sci Technol Weld Join* 26:136–143
52. El-Dasher BS, Adams BL, Rollett AD (2003) Viewpoint: experimental recovery of geometrically necessary dislocation density in polycrystals. *Scr Mater* 48:141–145
53. Kundu A, Field DP (2016) Influence of plastic deformation heterogeneity on development of geometrically necessary dislocation density in dual phase steel. *Mater Sci Eng A* 667:435–443
54. Li CM, Tan YB, Zhao F (2020) Dynamic recrystallization behaviour of H13-mod steel. *J Iron Steel Res Int* 27:1073–1086
55. Yu Y, Lan L, Ding F, Wang L (2019) Mechanical properties of hot-rolled and cold-formed steels after exposure to elevated temperature: a review. *Constr Build Mater* 213:360–376

56. Santillana B, Boom R, Eskin D, Mizukami H, Hanao M, Kawamoto M (2012) High-temperature mechanical behavior and fracture analysis of a low-carbon steel related to cracking. *Metall Mater Trans A Phys Metall Mater Sci* 43:5048–5057
57. Wang Y, Tsutsumi S, Kawakubo T, Fujii H (2021) Microstructure and mechanical properties of weathering mild steel joined by friction stir welding. *Mater Sci Eng A* 823:141715
58. Sun T, Wu SY, Shen Y, Jin JY, Lu JZ, Qin TX (2020) Effect of traverse speed on the defect characteristic, microstructure, and mechanical property of friction stir welded T-joints of dissimilar Mg/Al alloy. *Adv Mater Sci Eng* 2020:1–15
59. Zhou L, Zhang RX, Yang HF, Huang YX, Song XG (2018) Microstructure and mechanical properties of friction stir welded Q235 low-carbon steel. *J Mater Eng Perform* 27:6709–6718
60. Azizieh M, Mazaheri M, Balak Z, Kafashan H, Kim HS (2018) Fabrication of Mg/Al₁₂Mg₁₇ in-situ surface nanocomposite via friction stir processing. *Mater Sci Eng A* 712:655–662
61. Veiga RGA, Goldenstein H, Perez M, Becquart CS (2015) Monte Carlo and molecular dynamics simulations of screw dislocation locking by Cottrell atmospheres in low carbon Fe-C alloys. *Scr Mater* 108:19–22
62. Yu H, Yan Y, Zhang C, Qiao L (2023) Novel bake hardening mechanism for bainite-strengthened complex phase steel. *J Mater Sci Technol* 143:117–128
63. Wilde J, Cerezo A, Smith GDW (2000) Three-dimensional atomic-scale mapping of a Cottrell atmosphere around a dislocation in iron. *Scr Mater* 43:39–48
64. Ashrafi H, Sadeghzade S, Emadi R, Shamanian M (2017) Influence of heat treatment schedule on the tensile properties and wear behavior of dual phase steels. *Steel Res Int* 88:1–11
65. Huang GQ, Chou TH, Liu SF, Xiao B, Ju J, Gan J, Yang T, Zhang P, Yang JX, Lu CY, Meng FQ (2023) Unveiling the microstructure evolution and mechanical properties of submerged friction stir welded joint of fine-grained NiCoCr medium entropy alloy. *Mater Charact* 200:112903

Publisher's Note Springer Nature remains neutral with regard to jurisdictional claims in published maps and institutional affiliations.

Springer Nature or its licensor (e.g. a society or other partner) holds exclusive rights to this article under a publishing agreement with the author(s) or other rightsholder(s); author self-archiving of the accepted manuscript version of this article is solely governed by the terms of such publishing agreement and applicable law.